Experiments and Simulations of an Accelerating Buoyancy-Driven Model

J.S.Y Yen, D. Butler, D. Lamos, J. Seers, D.B. Clarke, R. Cairns, M. Rowan and A. Skvortsov

Maritime Division
Defence Science & Technology Group, Melbourne, Victoria 3207, Australia

Abstract

A preliminary experimental and numerical investigation of a buoyancy-driven model was conducted to develop the capability to computationally model accelerating bodies and predict the associated unsteady motion and hydrodynamic loads. The experimental and numerical models, setup and methods are described in detail. Additionally, the numerical acceleration model is first verified with the classic case of a falling sphere, and then validated against experimental data. For the buoyancy-driven model, comparison of the experimental data to the Computational Fluid Dynamics simulation revealed the latter over-predicted the acceleration, but overall still exhibited the same behaviour as the experiments. Possible sources for the discrepancy are discussed. The experimental and numerical results have informed future test programs, new buoyancy-driven model designs and improved computational methods to further develop capability to simulate flows around highly accelerating bodies.

Introduction

Buoyancy-driven models (BDMs), as their name suggests, are models that are propelled through water driven only by their buoyancy without any moving mechanical componentry [4]. Thus, without motors that are necessary to propel a model or generate flows around objects in wind and water tunnels, they are ideal for investigating flow noise produced by the BDMs themselves once they have attained their terminal velocity [6, 7]. To maximise the experimental measurement period, BDMs achieve their terminal velocity quickly and consequently have high accelerations. This makes them equally suitable for studying flows around accelerating bodies, such as rockets and torpedoes. In particular, the hydrodynamic loads on highly accelerating surface and subsurface naval platforms during manoeuvres can be significant, and thus their prediction important to both the platforms' performance and structural design.

Experimental results obtained during the acceleration phase of a preliminary BDM are presented, along with complementary computational results. These experimental results were used to provide validation data for the Computational Fluid Dynamics (CFD) simulation.

Experimental Description

Buoyancy-Driven Model

The BDM employed in the experiments is shown in figure 1, with large white dots on its surface for motion tracking. The axisymmetric body had a length of $L = 430$ mm and a semi-elliptical profile with a maximum diameter of 300 mm located 150 mm from the tip. Three fins of 50 mm chord and span lengths and 30° forward sweep, made from 1 mm thick aluminium sheet, were glued to the bottom of the body. A sting with 90 mm length and 6.25 mm diameter was screwed to the aft end of the body and used to hold the BDM in the release mechanism. The BDM total mass (body and sting) was measured to be $m = 0.25$ kg $\pm$ 0.86% using a Sartorius I12000S-X scale. The total volume, computed from CAD drawings and measured in a water bucket, was found to be $V = 1.49$ L $\pm$ 1.7%.
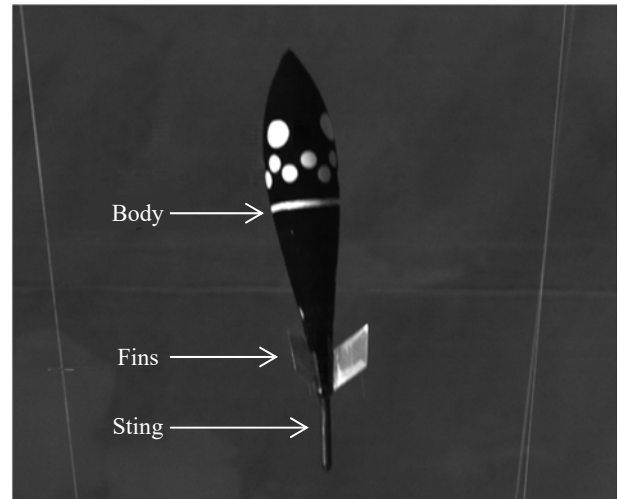
Figure 1. The buoyancy-driven model in the Defence Science and Technology Group's Large Water Tank.

Experimental Setup

Experimental testing was conducted in the Defence Science and Technology Group's Large Water Tank, which has a length, width and depth of 10 m x 10 m x 6 m, respectively. The release mechanism for the BDM consisted of two Danfoss BG024DS solenoids connected physically in series and mounted atop a box. A ring rigged with polystyrene buoys floated on the water surface, and suspended the release mechanism in the water with three lightweight strings.

A Photron FASTCAM SA-Z Type 480K monochromatic high-speed camera with 1024 px x 1024 px resolution and 12-bit dynamic range was used with a 50 mm lens to capture the motion of the BDM at a recording rate of 1000 Hz. The camera was aligned perpendicular to a viewing window at the bottom of the tank which had minimal perspective and barrel distortion. Calibration of the camera was performed by taking images of a graduated vertical pole placed at known locations within the tank.

Experimental Procedure

For each of the seven experimental runs, the release mechanism was first raised to the surface by supplying air through a hose to the suspended box. The BDM sting was inserted into the solenoids which were subsequently magnetised, powered by two 12 V lead-acid car batteries connected electrically in series. The release mechanism, together with the BDM, was then lowered into the tank by venting air from the box to atmosphere through the supply hose. After allowing the releasing mechanism, box and suspending ring to settle, the BDM was released by cutting power to the solenoids. Simultaneously, a 5 V TTL step signal was supplied to trigger recording by the camera.

Post-Processing

A calibration transformation matrix was first obtained from the calibration images. Then, for each image in every run, two of the large white dots were identified, their centroids computed, and the calibration transformation matrix applied to correct for perspective distortion and scale the pixel location to physical location. The displacement of the dots from the starting position was subsequently calculated.

The BDM motion was computed by averaging the displacement over all the runs, and then applying a Savitzky–Golay filter [9] of order 1 and window length of 15. The BDM speed was obtained by central differencing the averaged displacement, and then applying the same Savitzky–Golay filter. The BDM acceleration, a, was finally calculated by central differencing its speed.

Numerical Simulations

Computational Domain

As the BDM, ideally, had a rotational symmetry of order 3 about its longitudinal axis, only one-third of the BDM was modelled as shown in figure 2. The computational domain, consisting of an inner and outer domain, extended $10L$ upstream and $20L$ downstream of the BDM body and $5L$ in the radial direction from the longitudinal axis. In the inner domain, a structured C-grid type mesh was created to wrap around the BDM and was embedded into an H-grid (c.f. figure 2). The inner domain extended $2L$ upstream and $5L$ downstream of the body and $1L$ in the radial direction. A non-conformal (matching) interface joined the inner to the outer domain with a 2:1 ratio. The inner domain contained 572, 378 and 87 grid points in the longitudinal, radial and circumferential directions, respectively, and had a first-cell wall height that produced a y^+ value of O(1) at the end of the simulation. The mesh contained a total of 10, 899, 625 cells.
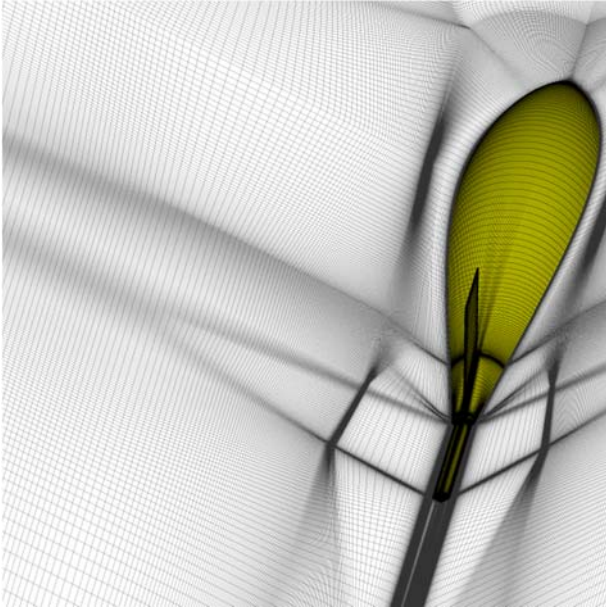
Figure 2. Surface mesh of BDM and symmetry boundaries.

Numerical Methods

The Unsteady Reynolds–Averaged Navier–Stokes equations were solved with the k–ω Shear Stress Transport turbulence model using ANSYS Fluent. The PISO algorithm was used to couple the pressure and velocity, and a second-order upwind scheme to spatially discretise all advection terms. The gradient terms were discretised and pressure interpolation carried out

with the Green–Gauss Cell-Based and second order methods, respectively, while temporal discretisation was achieved with a second-order implicit scheme with a constant timestep of $\Delta t = 1.0$ ms.

Boundary and Initial Conditions

The inlet and outlet boundaries were set as a pressure inlet and pressure outlet, respectively. The BDM body and sting were specified as no-slip walls, and symmetry boundary conditions set elsewhere. Due to the favourable pressure gradient over the forward portion of the BDM and small Reynolds number during the initial motion, a laminar zone was specified on the body between $0 \leq z/L \leq 0.384$, where z is the distance from the BDM nose and aligned with the longitudinal axis. The turbulent intensity was set to 2%, turbulent viscosity ratio to 4, gravitational acceleration to $g = 9.81$ m/s², water density to $\rho = 1000$ kg/m³ and water dynamic viscosity to $\mu = 1.003 \times 10^{-3}$ kg/ms. The flow was initialised as motionless.

Acceleration Model

To model the accelerating motion of the BDM, mesh motion was applied to the entire computational domain and controlled through a User Defined Function (UDF) that specified the mesh velocity, w. For the computed motion, a 1 degree-of-freedom (DOF) solver was employed to obtain the BDM acceleration:

$$\sum F_z = B - W - R = ma_z \qquad (1)$$

where $B = \rho V g$ is the buoyancy, $W = mg$ the BDM weight, and $R = F_D + F_{AM} + F_B$ the fluid resistance. The fluid resistance is composed of the drag, $F_D = \rho w^2 S C_D / 2$, added mass, $F_{AM} = C_{AM} \rho V a_z$, and Basset, F_B, forces, where S is the cross-sectional area, C_D the drag coefficient, and C_{AM} the added mass coefficient. The mesh velocity required for the UDF was obtained by numerically integrating the acceleration using the Forward Euler method:

$$w^{n+1} = w^n + a_z^n \Delta t \qquad (2)$$

where the superscripts n and $n+1$ are the values at the current and next timestep, respectively.

Timestep and Grid Independence

Timestep and grid dependence were investigated by halving both the timestep and the cells in the vicinity of the BDM in all three spatial dimensions using Fluent mesh adaption. The maximum instantaneous change in the BDM displacement, speed and acceleration after the initial oscillations had settled were 0.15%, 0.75% and 1%, respectively. The results from the original (coarser) mesh and timestep are therefore presented.

Verification of 1-DOF Solver UDF

To verify the 1-DOF solver UDF and its implementation in Fluent, two cases of a $D = 0.1$ m diameter and 1750 kg/m³ dense falling sphere accelerating under gravity from rest through quiescent, inviscid water were considered: the first without any retardation force, and the second with an artificial retardation force. The Basset-Boussinesq-Oseen equation [2, 5, 10] is typically used to describe the motion of a falling sphere, and is identical to equation (1) but with the buoyancy and weight terms having opposite signs. For these simulations, a structured O-grid was created around the sphere with 103 and 241 grid points in the radial and circumferential directions, respectively. The $40D$ diameter spherical computational domain modelled only a quarter of the sphere. The first-cell wall height produced a y^+ value of O(1) at the

sphere's terminal velocity of 1.4 m/s in the second verification case.

For the special case where $\mu = 0$ and a sphere accelerates through inviscid flow in the absence of any retardation force, $R = F_{AM}$ and the sphere undergoes a constant acceleration without achieving a terminal velocity. This was the first verification case considered. In this simulation, the pressure force on the sphere represented only the added mass force and was included in the 1-DOF solver. The computed constant acceleration corresponded to an added mass coefficient of $C_{AM} = 0.5006$. This was very close to the theoretical added mass coefficient for an accelerating sphere in potential flow of $C_{AM,theoretical} = 0.5$ [1].

The second case verified the 1-DOF solver UDF and its implementation in Fluent against the analytical solution of Guo [3] with $C_D = 0.5$ and $C_{AM} = 1$. Thus, an artificial retardation force was applied through the drag force term of equation (1) and was proportional to the sphere's velocity. Furthermore, specifying the above drag and added mass coefficients nominally accounted for the drag and added mass forces in equation (1). Consequently, in this simulation, the pressure force on the sphere calculated by Fluent was excluded from the 1-DOF solver. The computed motion of the sphere matched Guo's analytical solution.

Validation

Similar to the verification cases above, validation of the 1-DOF solver UDF in Fluent was performed by numerically simulating the falling sphere of Moorman [8] and comparing the results to his experimental data. Briefly, the experiment involved a $D = 0.0127$ mm diameter and 7780.22 kg/m^3 dense sphere falling from rest in oil with a density of 876.144 kg/m^3 and a kinematic viscosity of 1.078×10^{-5} m^2/s. The mesh used was the same as that for the verification cases but scaled down to the appropriate size. Figure 3 shows the velocity of the falling sphere against its displacement as measured by Moorman with black markers, and as computed from the CFD simulation in red. Overall, the numerical result agrees well with Moorman's experimental data. The slight over-prediction in velocity may be due to the first-order Forward Euler method used (see equation (2)) to numerically integrate the acceleration to obtain the velocity.
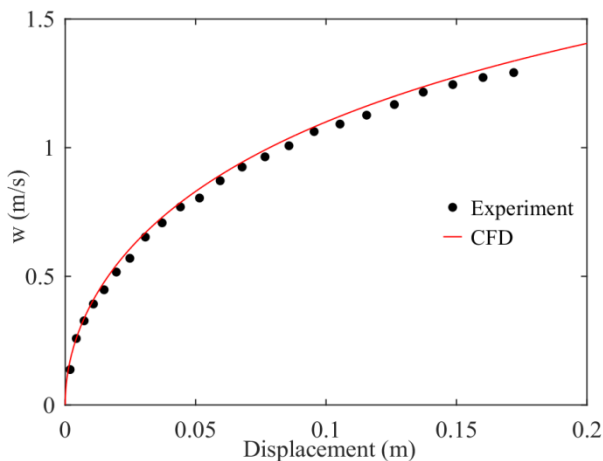
Figure 3. Velocity–displacement relationship of falling sphere from experiments by Moorman [8] (black) and CFD simulation (red).

Results & Discussion

The experimental BDM acceleration calculated from the high-speed camera images is shown in black in figure 4. The figure reveals the BDM accelerated, unexpectedly, slowly at the

beginning of its motion and, instead of at the instant of its release, achieved its maximum acceleration of approximately $a \approx 26.5$ m/s^2 around $t \approx 0.095$ s. This was also the time at which the BDM had moved the length of its sting and cleared the release mechanism. Consequently, the slow initial acceleration, $t < 0.03$ s, was primarily attributed to the release mechanism. It was believed that friction and/or eddy currents between the BDM's sting and the release mechanism solenoids decreased the initial acceleration. Tests of other buoyancy-driven models, not reported here, supported this hypothesis. These models also exhibited slow accelerations after being released, and achieved their maximum acceleration at approximately the time at which their sting had cleared the release mechanism.
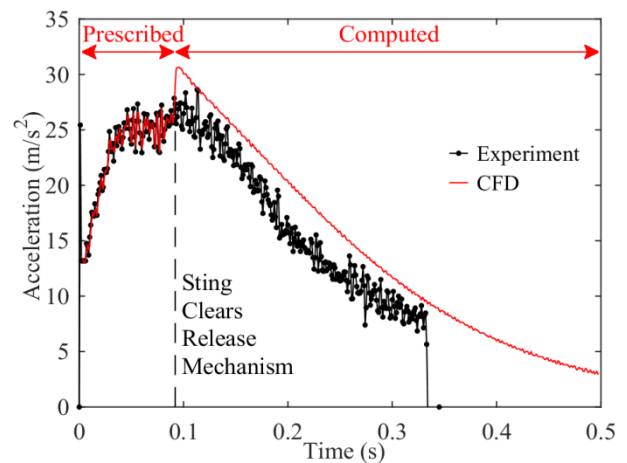
Figure 4. Acceleration time-history of the BDM from experiments (black) and CFD simulation (red). Dashed line indicates time at which the BDM sting cleared the release mechanism solenoids.

After the BDM had cleared the release mechanism and attained its maximum acceleration, its acceleration slowly decreased to approximately $a \approx 8$ m/s^2 at $t = 0.331$ s, after which it moved out of the camera's field of view.

For the CFD simulations, the BDM motion was initially prescribed according to the experimental data as the retarding frictional and/or electromagnetic effects between the sting and release mechanism solenoids were not modelled. This enabled the flow to develop in a manner similar to the experiments during the initial motion. Once the sting had cleared the release mechanism, $t > 0.092$ s, the BDM motion was then computed using the 1-DOF solver UDF described earlier. The periods of prescribed and computed motion are shown at the top of figure 4.

The acceleration calculated from the CFD simulation is shown in red in figure 4. As expected, the acceleration was identical to that in the experiments during the prescribed period. However, the acceleration suddenly and discontinuously increased from $a_z \approx 26.5$ m/s^2 to 30.5 m/s^2 when the BDM motion was switched from prescribed to computed at $t = 0.093$ s. The BDM acceleration subsequently decreased slowly, at a similar rate to the experiments, for the remainder of the computed motion.

The lesser acceleration calculated from the experimental high-speed camera images compared to the CFD simulation was attributed, mainly, to the experimental model having a significant degree of asymmetry. In the CFD simulation, the BDM had perfect rotational symmetry of order 3 and moved vertically upwards. In the experiments, however, the sting was misaligned with the body. Additionally, the manufacture and

attachment of the fins was imprecise. Close inspection of the BDM revealed one of the fins had a slight curvature (i.e. camber) and another was not parallel to the BDM longitudinal axis (i.e. had a small angle of incidence). These irregularities caused the BDM to "kick" sideways; to the left in figure 1. This sideways motion would have generated extra drag and, consequently, reduced the acceleration.

The reduced acceleration in the experiments may also be attributed to the experimental model having a non-hydrodynamically smooth surface. The BDM had a battered surface as a result of it exiting the Large Water Tank at its terminal velocity of approximately 8 m/s and impacting hard surfaces. This damage, along with the experimental model's inherent surface roughness of approximately 2.5 μm, would have increased the drag and decreased the measured acceleration, compared to the CFD simulation which modelled an intact and hydrodynamically smooth surface.

Finally, some of the discrepancy in acceleration between the CFD simulation and experiment may also be attributed to the 1-DOF solver itself. Similarly to the over-predicted velocity of Moorman's sphere shown in figure 3, the first-order Forward Euler method used in the 1-DOF solver would have over-predicted the acceleration in the simulation compared to the experiments.

Conclusions

Experimental and complementary numerical results of a preliminary investigation into the acceleration of a BDM are reported in this paper.

Experiments were conducted in the Defence Science and Technology's Large Water Tank, and a high-speed camera was used to track the BDM position. The BDM was found to initially accelerate slowly. It attained its maximum acceleration after its sting had cleared the release mechanism, after which its acceleration slowly decreased. The slow initial acceleration was attributed to friction and/or residual magnetic fields between the sting and release mechanism solenoids. A CFD simulation of the experiment was performed using Fluent. The BDM motion was incorporated by rigidly moving the entire computational domain. The velocity of the domain was controlled through a 1-DOF solver UDF. The motion was initially prescribed, as the frictional and electromagnetic effects were not modelled, before the 1-DOF solver was enabled. While the acceleration was greater than the experiments during the period of computed motion, the acceleration overall exhibited the same behaviour as the experiment and slowly decreased. The discrepancy between the experiments and CFD simulation was attributed to the experimental model containing a significant degree of asymmetry due to its manufacture and having a rough, battered surface, and to the first-order Forward Euler numerical integration method used in the 1-DOF solver.

The results have demonstrated that the present numerical methodology of moving the entire computational domain combined with a 1-DOF solver UDF can be utilised to specify rigid body motion and simulate flows around highly accelerating bodies.

The experimental and numerical techniques employed in this preliminary investigation are being further developed. A new buoyancy-driven model has been designed with a well-defined cylindrical body and NACA profile fins. This model is currently being manufactured. It will also be instrumented with inertial measurement units to complement the high-speed camera images. Additionally, a new release mechanism has been designed and manufactured that eliminates the frictional and electromagnetic effects that were present in the current solenoid-based release mechanism. Finally, a higher-order numerical integration method is being implemented in the 1-DOF solver UDF to enhance the accuracy of the motion predicted in future CFD simulations.

The ongoing complementary experimental and numerical investigation of buoyancy-driven models will allow improved validation and better understanding of flows around highly accelerating bodies. This is important to characterise the hydrodynamic loads and performance of naval platforms performing manoeuvres.

References

[1] Brennen, C.E. (1982). A Review of Added Mass and Fluid Inertial Forces. Port Hueneme, CA, Naval Civil Engineering Laboratory.

[2] Chang, T.J. and Yen, B.C., Gravitational Fall Velocity of Sphere in Viscous Fluid, *Journal of Engineering Mechanics*, **124**, 1998, 1193-1199.

[3] Guo, J., Motion of Spheres Falling through Fluids, *Journal of Hydraulic Research*, **49**, 2011, 32-41.

[4] Haddle, G.P. and Skudrzyk, E.J., The Physics of Flow Noise, *Journal of the Acoustical Society of America*, **46**, 1969, 130-157.

[5] Jalaal, M., Ganji, D.D. and Ahmadi, G., Analytical Investigation on Acceleration Motion of a Vertically Falling Spherical Particle in Incompressible Newtonian Media, *Advanced Powder Technology*, **21**, 2010, 298-304.

[6] Kudashev, E.B., Experimental Studies of Flow Noise around a Surfacing Device, *Acoustical Physics*, **51**, 2005, 414-424.

[7] Kudashev, E.B., Kolyshnitsyn, V.A., Marshov, V.P., Tkachenko, V.M. and Tsvetkov, A.M., Experimental Simulation of Hydrodynamic Flow Noises in an Autonomous Marine Laboratory, *Acoustical Physics*, **59**, 2013, 187-196.

[8] Moorman, R.W., *Motion of a Spherical Particle in the Accelerated Portion of Free Fall*, PhD Thesis, Department of Mechanics and Hydraulics, University of Iowa, 1955.

[9] Orfanidis, S.J., *Introduction to Signal Processing*, Englewood Cliffs, NJ, Pearson Education, 1996.

[10] Pantaleone, J. and Messer, J., The Added Mass of a Spherical Projectile, *American Journal of Physics*, **79**, 2011, 1202-1210.